Bioactive Materials 46 (2025) 21–36

Contents lists available at ScienceDirect

Bioactive Materials

journal homepage: www.keaipublishing.com/en/journals/bioactive-materials

Enhancing bone regeneration through 3D printed biphasic calcium phosphate scaffolds featuring graded pore sizes

Yue Wang [a,b,1], Yang Liu [c,1], Shangsi Chen [b,1], Ming-Fung Francis Siu [d], Chao Liu [c,**], Jiaming Bai [a,*], Min Wang [b,***]

[a] Department of Mechanical and Energy Engineering, Southern University of Science and Technology, Shenzhen, 518055, China
[b] Department of Mechanical Engineering, The University of Hong Kong, Pokfulam Road, Hong Kong, China
[c] Department of Biomedical Engineering, Southern University of Science and Technology, Shenzhen, 518055, China
[d] Department of Building and Real Estate, the Hong Kong Polytechnic University, Hung Hom Kowloon, Hong Kong, China

ARTICLE INFO

Keywords:
3D printing
Pore size graded scaffold
Mechanical property
Mass transport property
Bone tissue engineering
Vascularization
Osteogenesis

ABSTRACT

Human long bones exhibit pore size gradients with small pores in the exterior cortical bone and large pores in the interior cancellous bone. However, most current bone tissue engineering (BTE) scaffolds only have homogeneous porous structures that do not resemble the graded architectures of natural bones. Pore-size graded (PSG) scaffolds are attractive for BTE since they can provide biomimicking porous structures that may lead to enhanced bone tissue regeneration. In this study, uniform pore size scaffolds and PSG scaffolds were designed using the gyroid unit of triply periodic minimal surface (TPMS), with small pores (400 μm) in the periphery and large pores (400, 600, 800 or 1000 μm) in the center of BTE scaffolds (designated as 400-400, 400–600, 400–800, and 400–1000 scaffold, respectively). All scaffolds maintained the same porosity of 70 vol%. BTE scaffolds were subsequently fabricated through digital light processing (DLP) 3D printing with the use of biphasic calcium phosphate (BCP). The results showed that DLP 3D printing could produce PSG BCP scaffolds with high fidelity. The PSG BCP scaffolds possessed improved biocompatibility and mass transport properties as compared to uniform pore size BCP scaffolds. In particular, the 400–800 PSG scaffolds promoted osteogenesis *in vitro* and enhanced new bone formation and vascularization *in vivo* while they displayed favorable compressive properties and permeability. This study has revealed the importance of structural design and optimization of BTE scaffolds for achieving balanced mechanical, mass transport and biological performance for bone regeneration.

1. Introduction

Bone tissue engineering (BTE) holds great promise for treating bone defects because it can address various difficult issues associated with autografts and allografts while offering high biofunctionality [1,2]. By employing a viable BTE strategy that integrates scaffolds, growth factors and cells, the bone tissue could be regenerated inside the body with full functions in a regulated manner [3,4]. In recent years, biomimicking scaffolds have gained much attention as it is believed that scaffolds possessing similar geometrical features to those of native bone could have better ability and efficiency for bone regeneration [5–7]. Natural human long bones exhibit heterogeneous structures with porosity and pore size gradients from the peripheral cortical bone to central cancellous bone [8,9]. The cortical bone is highly compact with less than 10 % porosity, ensuring sufficient mechanical properties [10]. The inner cancellous bone consists of an irregular trabecular network, with a higher porosity ranging from 50 % to 90 % and pore diameters ranging from 100 to 1000 μm [11,12]. This porous region offers interconnecting channels for nutrient transportation and metabolic activities [13]. The combination of cortical bone and cancellous bone builds a favorable environment for cell activities and provision of normal bone functions. In this context, functionally graded scaffolds (FGS) should be developed

Peer review under the responsibility of KeAi Communications Co., Ltd.
* Corresponding author.
** Corresponding author.
*** Corresponding author.
E-mail addresses: liuc33@sustech.edu.cn (C. Liu), baijm@sustech.edu.cn (J. Bai), memwang@hku.hk (M. Wang).
[1] These authors contributed equally to this work.

https://doi.org/10.1016/j.bioactmat.2024.11.024
Received 22 May 2024; Received in revised form 19 September 2024; Accepted 18 November 2024

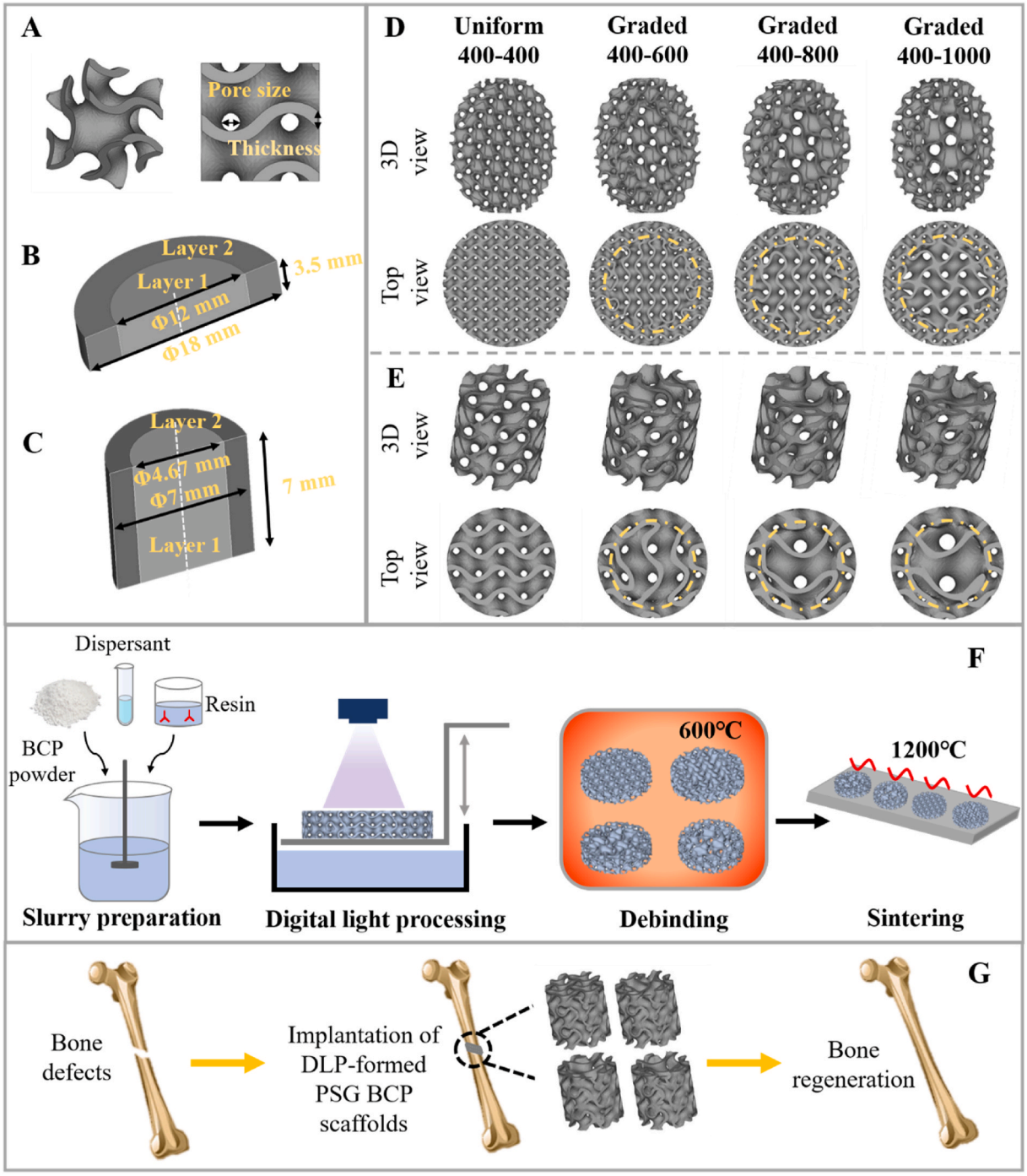

Fig. 1. Design, manufacture and application of PSG BCP scaffolds: (A) Geometrical features and definitions of pore size and thickness of the gyroid structure. Scaffold models with two layers of graded pore distributions are shown for (B, D) *in vitro* biological evaluations and for (C, E) compressive properties, mass transport characteristics, and *in vivo* biological evaluations. (F) Schematic diagram illustrating the fabrication process of BCP scaffolds via digital light processing (DLP) 3D printing. (G) Schematic diagram illustrating bone regeneration by using DLP-formed PSG BCP scaffolds.

for BTE since they can provide biomimicking features that may elicit desired mechanical and biological responses [14,15]. Zhang et al. presented a parametric design method for FGS based on triply periodic minimal surface (TPMS) units and fabricated the designed scaffolds using selective laser melting (SLM) with Ti6Al4V powders [16]. These structurally graded scaffolds displayed tunable mechanical properties while not significantly deteriorating their permeability. Pagani et al. designed and fabricated uniform and structurally graded cobalt-chrome (CoCr) alloy lattice scaffolds via SLM and compared their mechanical properties and *in vitro* biological behaviors [17].Their results showed that both uniform and porosity-graded scaffolds provided a favorable environment for the attachment and proliferation of osteoblasts while the porosity-graded scaffolds improved stress distribution between the CoCr implant and the host bone. Inspired by sea urchin spines, Zhang et al. constructed FGS based on pentamode metamaterials and fabricated them using SLM with Ti6Al4V [18]. Their scaffolds possessing graded pore size distributions exhibited suitable mechanical strength and showed great improvements in cell seeding efficiency, impact-tolerant capacity, permeability, and *in vivo* osteogenesis. Generally, compared to uniform scaffolds, FGS enable flexible control of

structural parameters and provide more possibilities for tuning the comprehensive performance of scaffolds by incorporating various types of graded features and gradient distributions. However, current BTE scaffolds are still mostly homogeneous porous structures due to various limitations in traditional fabrication methods [19]. Even with the opportunities and manufacturing platforms provided by 3D printing technologies, research on FGS is still in the very early stage and has primarily focuses on investigating FGS mechanical properties. Additionally, current FGS are mainly metallic scaffolds made by powder bed fusion (PBF) 3D printing technologies and cause inherent concerns of metallic materials as bone grafts, such as inflammation and implant loosening, mechanical instability, and poor implant integration with native tissues [20,21].

Biphasic calcium phosphate (BCP), a physical mixture of hydroxyapatite (HAp) and β-tricalcium phosphate (β-TCP), has been shown to be a good bone substitute bioceramic and is considered suitable for constructing BTE scaffolds because it is similar in mineral composition to natural bone and possesses sufficient biocompatibility, bioactivity, osteoconductivity, and biodegradability [22–24]. However, owing to their hard and brittle nature, ceramic materials such as BCP make it difficult to be shaped and processed post-device manufacture, particularly for customized, complex, and porous structures [25]. Digital light processing (DLP) 3D printing technology has proven to be a powerful manufacturing platform for processing ceramic materials into desired architectures with high controllability and reproductivity. It is currently a promising way for fabricating BTE scaffolds due to its high design freedom, resolution, accuracy, and desirable mechanical properties [26–28]. Additionlly, BCP scaffolds fabricated via the DLP process have exhibited good biocompatibility and superior bone-forming ability in previous studies [29,30].

Geometrical features of BTE scaffolds, such as pore size, pore morphology and porosity, exert a direct influence on the efficiency of bone regeneration [31,32]. Advances in computer-aided design and 3D printing technologies have opened up numerous ways for scaffold design and manufacture [33,34]. TPMS are a group of periodic implicit surfaces with zero mean curvature and smooth topology, which could offer controllable pore size, pore morphology and porosity by varying parameters in their mathematical equations. Recently, TPMS have been widely investigated for achieving biomimicking scaffolds due to their superior diffusion and permeability, less stress concentration and a high surface area to volume ratio as compared to traditional lattice or strut-based porous scaffolds [35–37]. Gyroid surface is triply periodic and consists of minimal iso-surfaces containing no straight lines [38]. Gyroid-based structure is self-supporting during the 3D printing process and is a frequently investigated TPMS structure for BTE scaffolds since its high tortuosity and inherent geometrical features may promote cell attachment and proliferation, as well as transportation of nutrients and oxygen [39,40]. Yang et al. showed that gyroid-based scaffolds could guide cell fate towards osteogenesis through cell-level directional curvatures [41]. In previous studies, it was shown that graded gyroid-gyroid scaffolds exhibited better dimensional accuracy, compressive properties, and cell proliferation than other three types of scaffolds investigated [42].

Considering the aforementioned advances and requirements, the objective of the current study was to investigate PSG BCP scaffolds by introducing pore size gradients while employing gyroid units of TPMS in scaffold design. The roles of graded pores in various scaffold properties would be systematically evaluated. Specifically, three types of PSG scaffolds, as well as uniform pore size scaffolds, were designed using computational design methods. Subsequently, scaffolds of the four designs would be fabricated through DLP 3D printing technology using BCP bioceramics. Thereafter, compressive properties, mass transport characteristics, *in vitro* and *in vivo* biological performances of the four types of scaffolds would be comprehensively evaluated and compared. This study would therefore explore and assess the strategy of developing high-performance BTE scaffolds through structural optimization and advanced 3D printing technology.

2. Materials and methods

2.1. Materials

Nano-sized HAp powders with a particle diameter of 20 nm and a length of 270 nm and near-spherical β-TCP powders with an average particle size of 500 nm were used as raw materials for making BCP for the current study. They were purchased from Nanjing Emperor Nano Material Co., Ltd. The organic reagents for preparing photosensitive BCP slurry, isobornl acrylate (IBOA), 1,6-Hexanediol diacrylate (HDDA), polyethylene glycol diacrylate (PEGDA) and 2,4,6-trimethylbenzoyldiphenyl phosphine oxide (TPO) were supplied by Shanghai Yinchang New Material Co., Ltd. A commercial dispersant, BYK 111 (BYK Chemie, Germany), was applied for slurry dispersion. All materials were used as-received without further processing.

2.2. Design and fabrication of PSG scaffolds and uniform pore size scaffolds

The graded gyroid-gyroid surfaces can be described by mathematic equations (provided in supplementary). The design procedures of PSG scaffolds were as follows: Firstly, the graded surfaces were created using MATLAB software. Subsequently, a thickness was added to these surfaces to generate 3D porous structures. Finally, Magics software was employed to adjust and convert the structures into standard stereolithography (.stl) files for 3D printing.

In the current study, four types of scaffold models with different pore size distributions were designed based on the gyroid unit. The definitions of pore size and thickness can be seen in Fig. 1(A). PSG scaffolds with radially varying pore sizes consisted of two layers, with a layer radius ratio of 2: 1. Two groups of models were designed for different research objectives, while maintaining same geometrical features, such as pore size gradient and porosity. The 3D models with a larger diameter were used for *in vitro* biological evaluations (Fig. 1(B) and D), whereas the taller models were employed to assess mass transport characteristics, compressive properties, and *in vivo* subcutaneous performance (Fig. 1(C) and E). Specifically, three types of PSG scaffolds possessed graded pore sizes from the scaffold periphery (pore size of 400 μm in all scaffold models) to the scaffold center (pore size of 600, 800 and 1000 μm), which were designated as 400–600, 400–800, and 400–1000 scaffold, respectively. Scaffolds with uniform pore sizes of 400 μm (the "400-400" scaffolds) were used as the control group. All scaffolds were designed to have the same porosity of 70 vol% by adjusting unit size and wall thickness.

All.stl files of scaffold models were imported into a custom-built ceramic DLP 3D printer. The fabrication process for BCP scaffolds via DLP 3D printing is illustrated by Fig. 1(F). First, a photocurable BCP ceramic slurry was prepared, which consisted of BCP powders with an HAp to β-TCP ratio of 50 % (wt./wt.), a resin matrix comprising IBOA, HDDA, PEGDA and TPO, and the dispersant BYK 111. The detailed BCP slurry formulation and preparation procedures could be found in our previous publication [42]. After DLP 3D printing, the green bodies were heated from room temperature to 600 °C, following a certain debinding profile to remove polymer phases. Finally, for sintering, the samples were heated to 1200 °C at a heating rate of 2 °C/min and were held at 1200 °C for 2 h in a furnace (LHT 04/17, Nabertherm, Germany). The current PSG BCP scaffolds were made for use in bone regeneration under bone defects conditions (Fig. 1(G)).

2.3. Morphological and structural analysis

The outward morphology and general pore architectures of sintered BCP scaffolds were observed and recorded using a digital camera. Micro-CT scanning was performed using a laboratory μ-CT system

(SKYSCAN1172, Bruker, Germany) at the following parameters: voltage, 60 kV; current, 100 μA. The voxel size of the dataset was set to 7 μm, and 0.5 mm aluminum foil was used to filter X-ray. Detailed pore characteristics of these four types of scaffolds were observed using scanning electron microscopy (SEM) (LSCM, VK-X1000, Keyence, Japan), and the pore sizes were measured using software Nanomeasure and SEM images of scaffolds. The size of scaffold samples in X-Y and Z dimension after sintering was measured using a digital vernier caliper (500-702-20, Mitutoyo, Kawasaki, Japan). The porosity of 3D models of these scaffolds was obtained using software Magics. The real porosities of final sintered scaffolds were calculated using the weight measurement method [43]. For each condition, at least five samples were tested for porosity calculation. The microstructure of BCP scaffolds was analyzed using SEM. X-ray diffraction (XRD) analysis was conducted to determine the phase constitution of sintered BCP scaffolds.

2.4. Compressive properties

The compression tests of sintered BCP scaffolds ($\varnothing 7\times 7mm, N=5$) were conducted using a universal mechanical testing machine at a loading speed of 0.25 mm/min. The compressive strength was obtained by the maximum stress value and Young's modulus was the slope of the linear part of the stress-strain curve. A Weibull analysis of the compressive strength data was conducted to estimate the failure probability of BCP scaffolds (at least 20 samples). A commercial software ANSYS Workbench was utilized to perform finite element analysis (FEA) to investigate the stress distribution and predict the cracking behavior of these four types of porous structures. Two rigid plates were tired to the top and bottom surfaces of the porous structures to ensure the simulation quality [44]. The density, Young's modulus, and Poisson's ratio of BCP were set to 3.15 g/cm^3, 7.51 GPa and 0.27, respectively. The density was determined based on the separate densities of HAp (3.16 g/cm^3) and β-TCP (3.15 g/cm^3), as well as the constitutional ratios after sintering [45]. The Young's modulus value was determined through compression tests conducted on non-porous solid BCP ceramics fabricated via current DLP 3D printing route. The Poisson's ratio of BCP was assumed based on reported papers [46,47]. A displacement of 1 % strain was applied to the top surface while the bottom was fixed as a boundary condition.

2.5. Mass transport characteristics

The mass transport characteristics in designed scaffolds were simulated through computational fluid dynamics (CFD) analysis using the Ansys Fluent software. Since Reynolds number was less than 1, a laminar CFD model was employed in the current study. The flow medium chosen for the simulation was water, which has a density of 1000 kg/m^3 and a dynamic viscosity (u) of 10 $^{-3}$ Pa s [48,49]. The inlet flow velocity (v) was set to be 0.001 m/s regarding the bone *in vivo* conditions while the outlet pressure was defined as zero [50,51]. The pressure drop (Δp) was defined as the difference between inlet and outlet pressures. The computational permeability was calculated using the following equation (50):

$$K_c = \frac{vul}{\Delta p} \tag{1}$$

where l is the model height.

A setup for permeability tests was established for studying experimentally the fluid flow behavior of porous BCP scaffolds. The flow rate was determined by measuring the volume of water flowing through the scaffolds within a certain period of time. Different water heights of 30, 40, 50, 60 and 70 mm resulting in pressure gradients ($\Delta p = \rho g h$) of 294, 392, 490, 588, and 686 Pa, respectively, were analyzed. The experimental permeability values were calculated according to Darcy's equation:

$$K_e = \frac{\mu q l}{A \Delta p} \tag{2}$$

where μ is the fluid viscosity, q is the fluid flow rate, l and A are length and cross-sectional area of the porous scaffolds, respectively.

To establish the relationship between CFD analysis results and experimental results for predicting the permeability of porous scaffolds, a correlation factor C was introduced to relate the computational permeability (K_c) to experimental permeability (K_e) at each fluid height (and hence pressure gradient):

$$k_e = C \times k_c \tag{3}$$

2.6. Cell culture

Mouse preosteoblasts cells (MC3T3-E1) were used in the current study to evaluate the *in vitro* biological properties of BCP scaffolds fabricated. They were purchased from the Cell Bank of the Chinese Academy of Sciences (CBCAS, China). MC3T3-E1 cells were cultured in α-minimum essential medium (α-MEM) supplemented with 10 % fetal bovine serum (FBS) and 1 % penicillin/streptomycin in a humidified atmosphere of 5 % CO_2 at 37 °C. The osteogenic differentiation medium contained the basic culture medium with 1 μM dexamethasone, 10 mM β-glycerophosphate, and 50 μg/mL ascorbic acid. The culture medium was refreshed every two days to ensure adequate nutrient supply for the cells.

2.7. Cell adhesion and proliferation

To observe cytoskeleton and spreading of MC3T3-E1 cells cultured on BCP scaffolds, cells at a density of 2.0 × 10^5 cells/well were seeded on the scaffolds and cultured for 1, 3, and 5 days, respectively. At each predetermined time point, cells were fixed with 4 % PFA for 20 min and washed three times using phosphate buffered saline (PBS). Then, cells were permeabilized with 0.5 % Triton X-100 for 10 min. Subsequently, cells were stained with rhodamine-phalloidin for 1 h to mark actin filaments and DAPI for 20 min to mark nucleus of the cells. All samples were observed under a laser scanning confocal microscope (LSM 980, ZEISS) in a reflected mod. An air objective lens with 20× magnification and a numerical aperture of 0.8 was used. Z-stacks of 100 μm height were taken at a size of 1024 × 1024 pixels, with an x−y resolution of 0.414 μm and a z-step of 2 μm. To further evaluate cell attachment on BCP scaffolds after incubation for 5 days, cell-scaffold samples were fixed by 4 % polyformaldehyde (PFA, Sigma-Aldrich, USA) for 30 min and subsequently dehydrated in a graded ethanol series from 30 %, 50 %, 75 %, 95 % and 100 % for 5 min each. The samples were then dried at room temperature and sputter-coated with gold for SEM observation.

Cell Counting Kit-8 (CCK-8) assay was used to assess cell viability and proliferation. After 1, 3 and 5 days of incubation, the cells were treated with CCK-8 solution for 1 h. The absorbance was then measured at 450 nm using a microplate reader.

2.8. In vitro osteogenic differentiation

To evaluate early osteogenic differentiation, alkaline phosphatase (ALP) activity was quantitively analyzed using ALP assay kits supplied by Nanjing Jiancheng Bioengineering Institute. Briefly, MC3T3-E1 cells at a density of 2.0 × 10^5 cells/well were seeded on different types of scaffolds and cultured in the osteogenic medium for 7 and 14 days. On day 7 and 14, cells were washed with PBS and then lysed in a lysis buffer for 30 min. The ALP activity and total protein concentration were determined following the instructions of the ALP assay kit and protein assay kit. Additionally, ALP staining was conducted at the same time points using an ALP staining assay kit (Beyotime, China). After cells were fixed with 4 % PFA for 30 min, the samples were stained with a 5-bromo-4-chloro-3-indolyl-phosphate (BCIP)/(nitro-blue-tetrazo-lium)

Table 1
Morphological parameters of two groups of BCP scaffolds.

Group 1	Uniform 400-400		Graded 400-600		Graded 400-800		Graded 400-1000	
	X-Y	Z	X-Y	Z	X-Y	Z	X-Y	Z
After printing/mm	22.34 ± 0.04	4.02 ± 0.02	22.34 ± 0.03	3.98 ± 0.02	22.34 ± 0.03	4.00 ± 0.03	22.31 ± 0.03	3.99 ± 0.03
After sintering/mm	18.56 ± 0.29	3.48 ± 0.06	18.62 ± 0.12	3.48 ± 0.04	18.67 ± 0.02	3.46 ± 0.04	18.59 ± 0.17	3.47 ± 0.05
Shrinkage/%	17.5	12.9	17.2	13.0	17.0	13.4	17.4	13.2
Porosity/%	67.8 ± 1.2		68.0 ± 0.6		69.6 ± 0.8		70.8 ± 1.0	
Central pore size/μm	391.7 ± 24.9		581.1 ± 26.8		799.5 ± 53.5		990.5 ± 26.5	
Group 2								
After printing/mm	8.71 ± 0.03	8.45 ± 0.01	8.69 ± 0.07	8.49 ± 0.04	8.68 ± 0.06	8.45 ± 0.05	8.69 ± 0.06	8.41 ± 0.06
After sintering/mm	7.16 ± 0.06	6.99 ± 0.07	7.14 ± 0.03	7.01 ± 0.11	7.13 ± 0.03	6.97 ± 0.07	7.12 ± 0.06	6.96 ± 0.04
Shrinkage/%	18.2	16.8	18.4	16.5	18.5	17.0	18.6	17.1
Porosity/%	71.1 ± 1.4		72.1 ± 0.5		72.5 ± 0.2		72.2 ± 0.6	
Central pore size/μm	390.6 ± 16.1		591.2 ± 28.7		805.2 ± 14.8		978.0 ± 32.6	

NBT solution for 30 min and then washed twice with ultrapure distilled water to terminate the reaction.

To assess calcium deposition by MC3T3-E1 cells on BCP scaffolds, Alizarin red staining and quantification were performed. Cells were seeded on BCP scaffolds and cultured with an osteogenic differentiation medium for 14 and 21 days. At each time point, the culture medium was removed and scaffolds were washed with PBS three times. After being fixed with 4 % PFA for 30 min, cell-scaffolds were incubated with Alizarin red solution (pH 4.2) for 30 min at 37 °C to stain mineralized calcium nodules. The staining morphology was captured using a digital camera. To quantitively analyze the staining results, the samples were dissolved in cetylpyridinium chloride and the absorbance was measured at 540 nm using a microplate reader.

Osteogenesis-related gene expression of MC3T3-E1 cells cultured on different types of scaffolds was investigated using a real-time quantitative PCR (RT-qPCR). In brief, MC3T3-E1 cells at a density of 2.0×10^5 cells/well were seeded on BCP scaffolds in 12-well plates for the 14-day osteogenic differentiation. The total cellular RNA was extracted using TRIZOL reagent (Invitrogen, USA) and transcribed into complementary DNA (cDNA) by applying a RevertAid First Strand cDNA synthesis kit (K1622, Thermo Fisher). The RT-qPCR analysis was performed using a QuantStudio 5 Real-Time PCR system (A34322, Thermo Fisher Scientific). The relative expression of genes including ALP and COL1 was calculated using the $2^{-\Delta\Delta CT}$ method with the normalization of housekeeping gene glyceraldehyde 3-phosphate dehydrogenase (GAPDH) [52]. The summary of genes and forward and reverse primers are listed in Table S1.

2.9. In vivo study

Mice were used in the *in vivo* study, and all animal study procedures were followed in accordance with the Institutional Animal Care and Use Committee (certificate SUSTC-JY 20190427). The ectopic osteogenesis and vascularization ability of fabricated BCP scaffolds were evaluated using a subcutaneous implantation model in C57BL/6J mice. All female mice weighing 20–25 g were obtained from the animal center of the

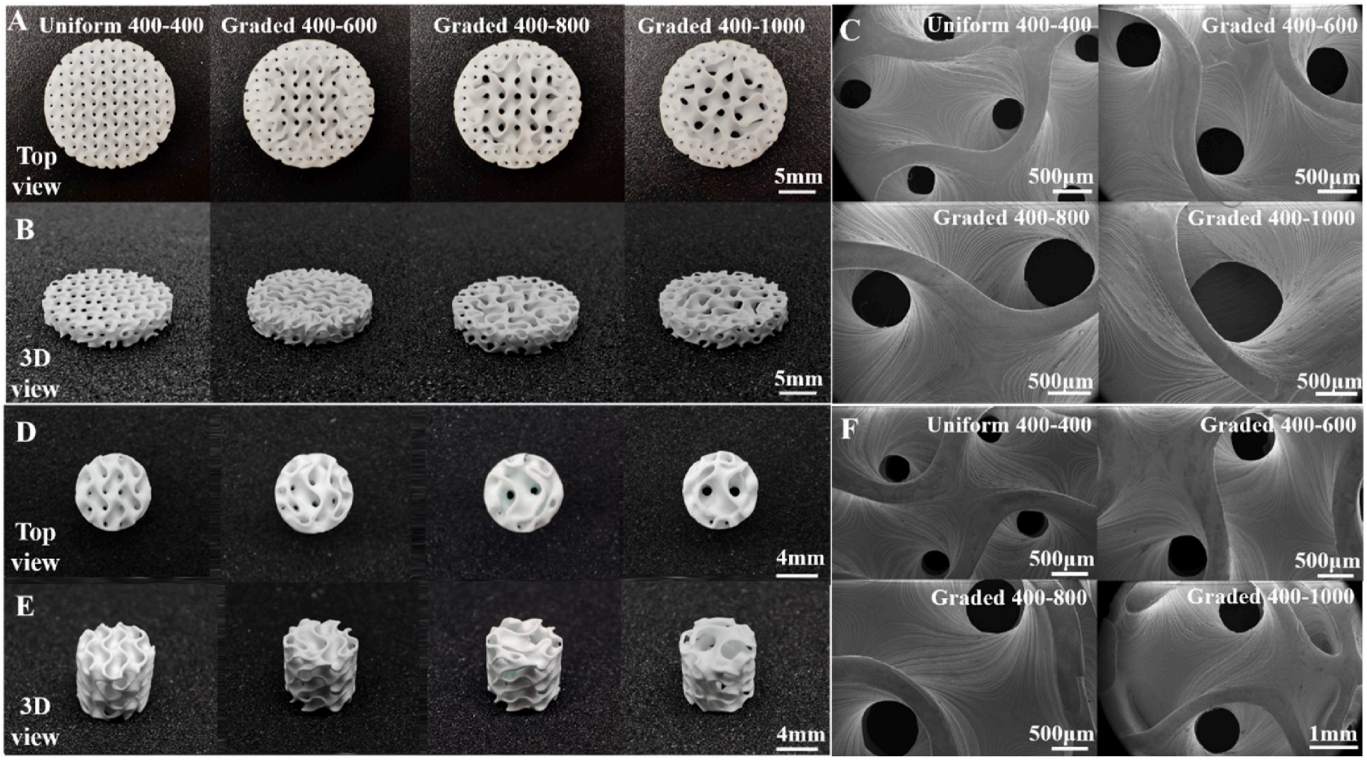

Fig. 2. Morphological characteristics of uniform pore size and PSG BCP scaffolds. Scaffolds for *in vitro* biological evaluations: (A) Top view. (B) 3D view. (C) SEM images of central pores. Scaffolds for compressive properties, mass transport characteristics and *in vivo* biological evaluations: (D) Top view. (E) 3D view. (F) SEM images of central pores.

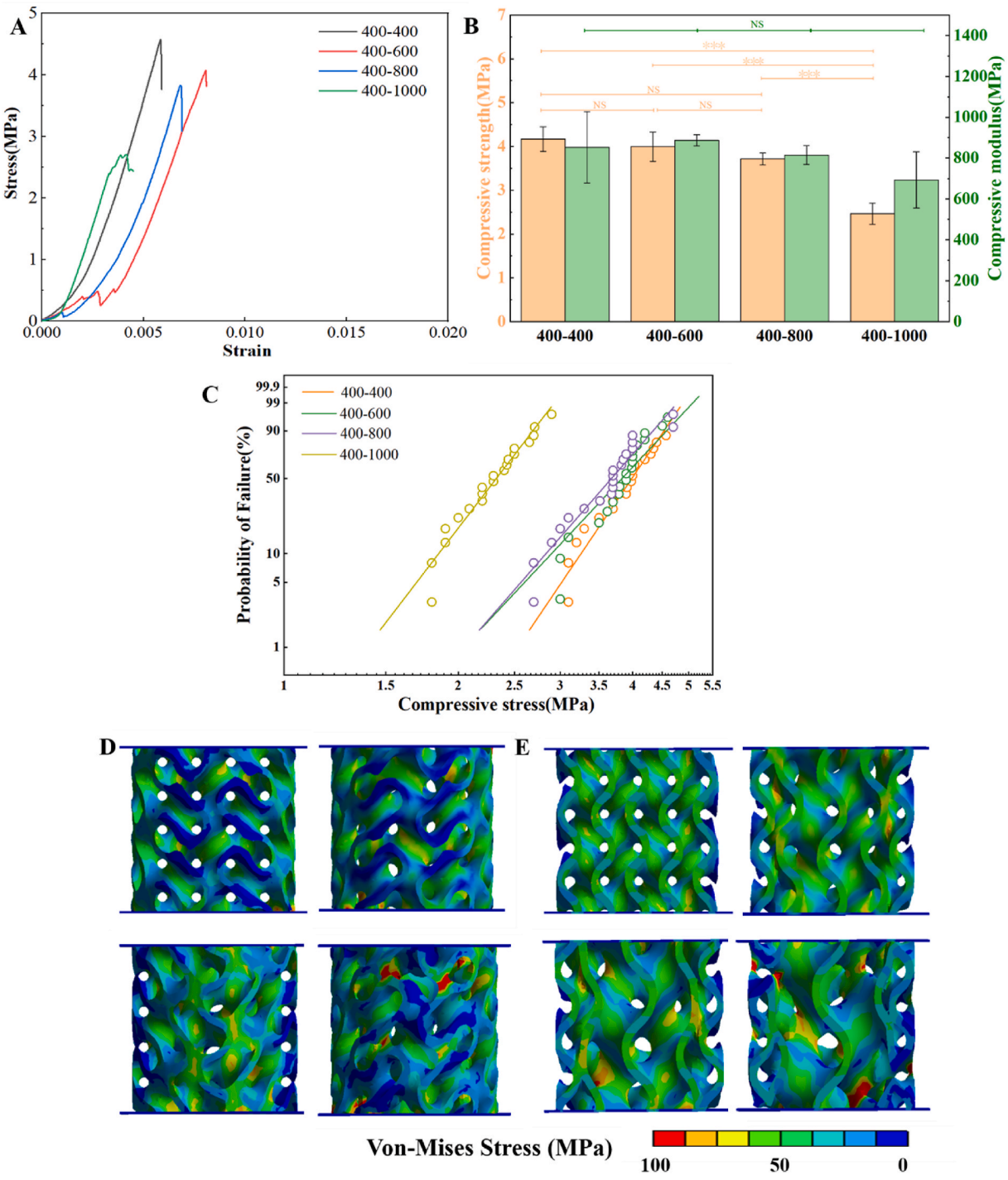

Fig. 3. Compression behavior and properties of uniform pore size and PSG BCP scaffolds analyzed through compression tests and finite element analysis (FEA): (A) Compressive stress-strain curves. (B) Compressive strength and modulus (NS: no significant difference. ***$p < 0.001$). (C) Weibull plot of the compressive strength. Stress distribution from (D) front view and (E) cross-sectional view.

University. During operation, each animal was anesthetized and maintained with inhalational isoflurane and oxygen. After shaving the dorsal area, two pockets were created on each side of the dorsum. After 2- and 4-week subcutaneous implantation, the samples were harvested, fixed in 4 % PFA for 24 h, and decalcified in a large volume of 19 % ethylenediaminetetraacetic acid (EDTA) at 4 °C for 3 weeks before tissue processing.

The tissue samples were dehydrated with gradient ethanol and embedded in paraffin (Leica ASP 300S, Leica). 14 μm paraffin tissue sections were created using a microtome (Leica CM1950, Leica) and stained with hematoxylin and eosin (H&E), and Goldner's Trichrome, according to the manufacture's protocols.

Immunohistochemical staining for vascular endothelial growth factor (VEGF) and cluster of differentiation 31 (CD31) was performed with the rabbit VEGF primary antibody (1:200, Abcam, AB46154) and mouse CD31 primary antibody (1:100, BD, BD553847), and then with the second antibody HRP goat anti-rabbit (GB23303, Servicebio, 1:200) and HRP goat anti-mouse (GB23301, Servicebio, 1:200). Images after staining were obtained under a light microscope (MF53-M, Mingmei). The number and positive-stained area of VEGF and CD31 were

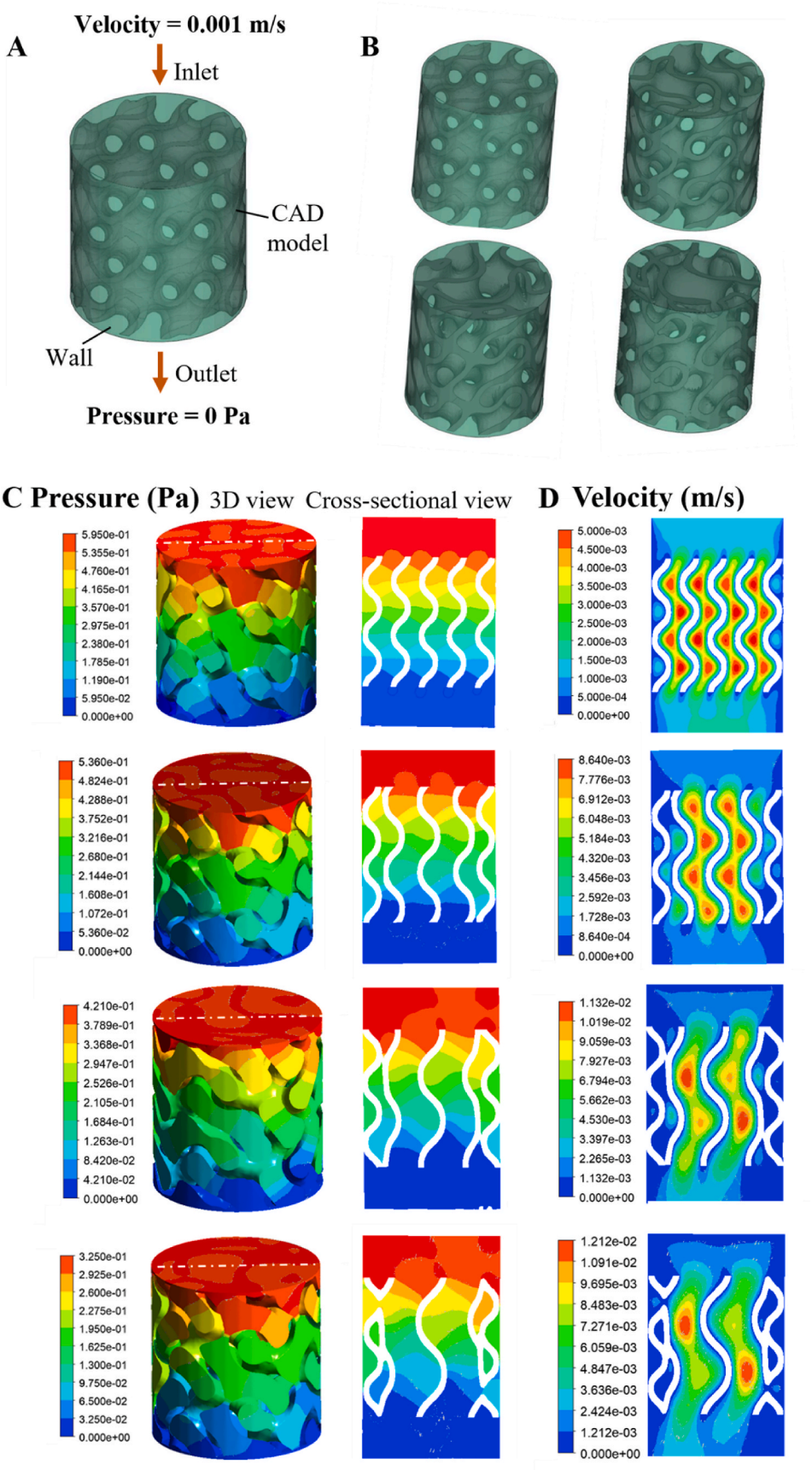

Fig. 4. Computational fluid dynamics (CFD) analysis of uniform pore size and PSG BCP scaffolds: (A) Boundary conditions and (B) schematic representation of models. (C) Pressure contours on scaffold surfaces and middle cross-sections. (D) Velocity distributions in middle cross-sections.

quantified at a magnification of 20 × using the Image J software.

2.10. Statistical analysis

The numerical data obtained in the current study were statistically analyzed using Origin software. All quantitative data was shown as mean ± standard deviation. Statistical analysis among various experimental groups was performed via one-way ANOVA, and independent t tests were used between two groups. Statistically difference was set at $^{*}p < 0.05$, $^{**}p < 0.01$, $^{***}p < 0.001$.

3. Results and discussion

3.1. Morphological and structural characteristics

Two groups of BCP scaffolds with uniform pore size and pore size gradients, respectively, were successfully fabricated via DLP 3D printing technology, as shown in Fig. (A–B, D-E). Micro-CT images (Fig. S1) indicated that the sintered scaffolds were consistent with the 3D designs. The detailed morphological parameters of the uniform pore size and PSG scaffolds after DLP 3D printing, after sintering, corresponding shrinkages, measured porosities, and central pore sizes are listed in Table 1. Shrinkage is a common issue for sintering in ceramic product fabrication and excessive shrinkage can result in defects or cracks in sintered products, thereby affecting the final properties of ceramics [53,54]. Group 1 and Group 2 showed a similar trend in shrinkage. Specifically, the shrinkage rates of the four types of scaffolds in each group were roughly the same in the X-Y or Z axis (17.5 % vs 17.2 % vs 17.0 % vs 17.4 % in the X-Y axis, 12.9 % vs 13.0 % vs 13.4 % vs 13.2 % in the Z axis). However, the differences in shrinkage between these two groups were more pronounced, particularly in the Z axis, with ~13.0 % in Group 1 and ~17.0 % in Group 2. The variation may stem from different temperature distributions within the structures of these two groups, possibly due to structural differences especially the porous geometries and sample heights [55]. The detailed pore features of central pores in the BCP scaffolds in the two groups are shown in Fig. 2 (C and F). It is evident that the gyroid-based pores were generated through the layer accumulation of curved surfaces whose centers kept changing in the plane during the printing [45]. These intrinsic characteristics of gyroid unit could induce cytoskeleton reorganization of human mesenchymal stem cells (hMSCs) and direct cell fate towards osteogenesis and angiogenesis [41]. Overall, the pore size, porosity, and overall dimensions of sintered scaffolds exhibited a high level of conformity with the desired 3D designs, demonstrating the high fidelity and controllability of the current DLP process for fabricating customized BCP scaffolds, which could be used for subsequent investigations. The surface microstructure of the sintered BCP is provided in Fig. S2. The ceramic grains were tightly connected to adjacent grains, indicating that BCP scaffolds with a high level of densification were achieved. BCP bioceramics fabricated via DLP process with a denser surface morphology were considered beneficial for cell adhesion and proliferation [56]. Therefore, the BCP scaffolds in the current study may also benefit bone cells behaviors. Furthermore, the phase constitution of sintered BCP scaffolds was analyzed via XRD, as shown in Fig. S3. After sintering, characteristic peaks of HAp and β-TCP were detected without any extraneous peaks, suggesting that the BCP scaffolds were only composed of HAp and β-TCP, which would provide the desired biocompatibility and bioactivity for BTE scaffolds.

3.2. Mechanical properties

Scaffold for BTE applications should possess sufficient compressive properties to withstand forces and support cell metabolisms after implantation. Fig. 3 (A) provides representative compressive stress-strain curves of four types of BCP scaffolds. All scaffolds exhibited a typical brittle fracture behavior of ceramic materials, with the compressive stress increasing as displacement increased in the early compression stage and then suddenly dropping when the fracture strain was reached. Some scaffolds (graded 400–600, indicated by the red curve) displayed a decrease in stress followed by an increase, which could be attributed to the presence of small cracks or defects within the scaffolds [57]. Fig. 3 (B) provides compressive strengths and modulus of the four types of scaffolds. The compressive strengths of uniform pore size 400-400 scaffolds and graded 400–600, 400–800 and 400–1000 scaffolds were 4.17 ± 0.28 MPa, 3.99 ± 0.33 MPa, 3.71 ± 0.14 MPa, and 2.46 ± 0.24 MPa, respectively. Notably, the compressive strengths of the 400-400, 400–600 and 400–800 scaffolds showed significant differences as compared to graded 400–1000 scaffolds, even though they possessed the same porosity. Pore size, porosity, and pore architectures directly influence the mechanical properties of scaffolds [58]. Zhao et al. investigated the effect of structural features, such as porosity, pore size and pore interconnectivity, on mechanical properties [59]. Their results revealed an obvious negative relationship between pore size and compressive strength. Smaller pore sizes within a honeycomb structure enhanced mechanical strength of porous scaffolds. Fig. 3(C) shows the Weibull plot of the compressive strength. The Weibull modulus of uniform 400-400 scaffolds and PSG scaffolds was 9.34, 6.47, 7.24, and 8.23, respectively, indicating the scaffolds were of high reliability [60,61].

To investigate the cracking behavior for uniform pore size and PSG scaffolds, the stress distribution in 3D models of four types of scaffolds was analyzed and compared using FEA under a boundary condition of a 1 % strain displacement. The 400-400 scaffolds exhibited a homogeneous stress distribution, whereas in PSG scaffolds, stress concentration occurred in regions with large curvature changes, especially in the transitional areas (Fig. 3(D and E)). This indicated that the realization of graded structure features through automatic combination using continuous equation may compromise the structural integrity and consequently affect the mechanical performance of the graded structures. Uniform pore size 400-400 scaffolds, graded 400–600 scaffolds and 400–800 scaffolds exhibited significantly improved compressive properties. This improvement can be attributed to the presence of smaller pore sizes in the outer region and well-designed transitional areas, which contribute to their ability to withstand applied loads effectively. However, the large red area in graded 400–1000 scaffolds could be regions prone to cracking under compressive loads.

3.3. Mass transport properties

The mass transport characteristics in porous scaffolds are highly related to the transportation of oxygen and nutrients, as well as waste emission, which greatly affects cell behaviors [62,63]. The boundary conditions and schematic representation of models for the CFD analysis are depicted in Fig. 4(A and B). Fig. 4(C) shows pressure contours on the 3D surfaces and middle cross-sections of the four types of scaffolds obtained from CFD analysis. The pressure distributions exhibited a high similarity for the four types of scaffolds owing to the utilization of gyroid units as the fundamental constitutional components, and they had a strong dependence on pore shape and morphology. It was noted that the pressure showed a linear decline from the inlet to the outlet, leading to variations in mass transport abilities. Fig. 4(D) displays velocity distributions in the middle cross-section of scaffolds. All porous scaffolds showed a consistent pattern in velocity distribution, wherein the velocity in pores in the center of scaffolds exceeded that in the outer surface. Particularly, the velocity was higher in those areas with larger pore sizes, which may increase the available surfaces for cell attachment [64]. With the increase of the central pore sizes, the velocity in the graded scaffolds increased correspondingly. An optimal fluid velocity can effectively promote osteogenesis, as the flow rate serves as a biomechanical stimulus that could enhance the proliferation and differentiation of bone cells [65,66].

In quantitively evaluating the mass transport abilities of uniform pore size scaffolds and PSG scaffolds in conducting fluid flow, both

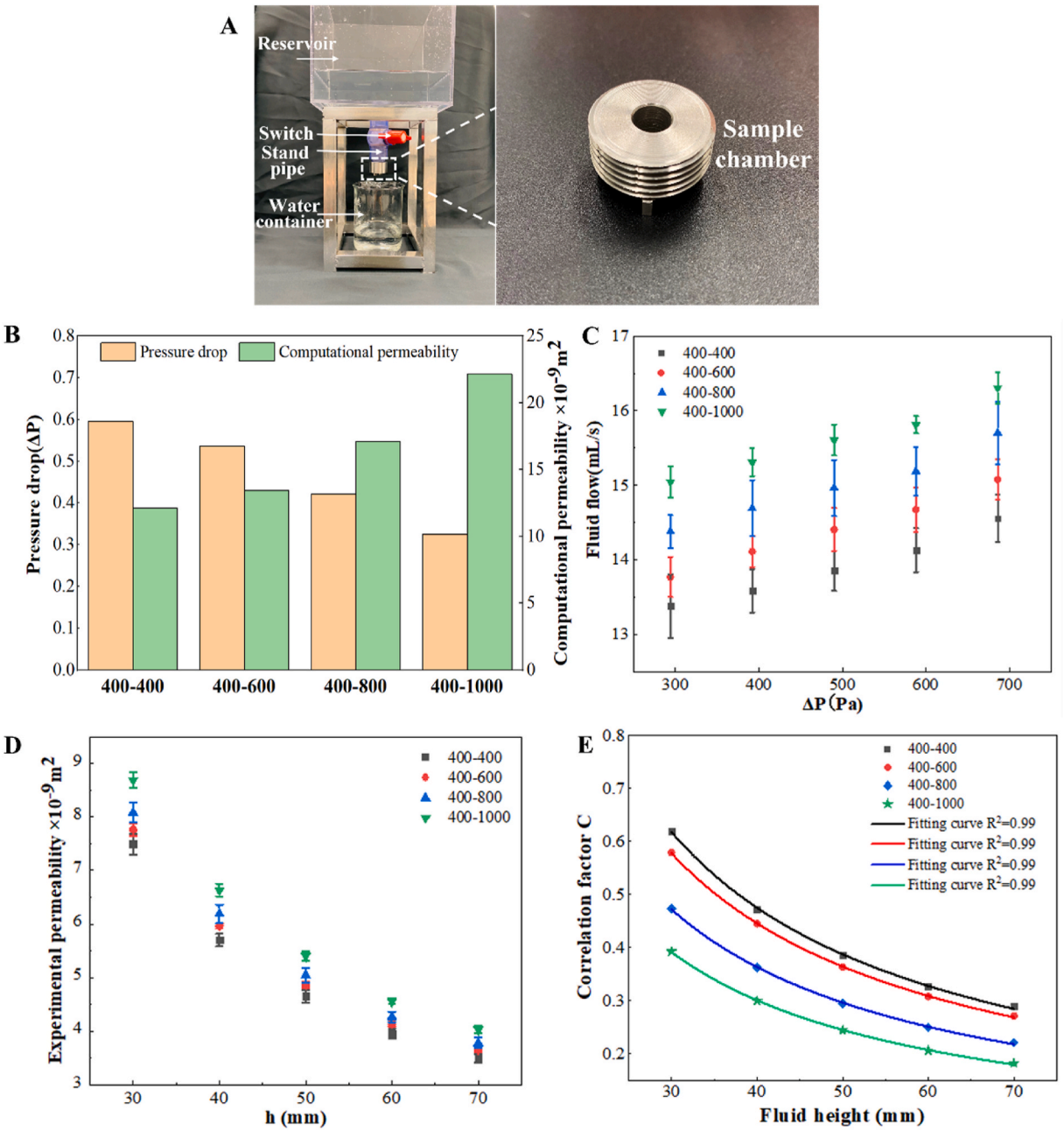

Fig. 5. Mass transport properties of uniform pore size and PSG BCP scaffolds: (A) Custom-made set up for permeability tests. (B) Pressure drop and computational permeability based on CFD analysis. (C) Experimental results of fluid flow versus pressure drop. (D) Experimental permeability versus fluid heights. (E) Correlation factors at different fluid heights and their fitting curves.

computational and experimental permeabilities were calculated. The test setup for experimental permeability analysis is shown in Fig. 5(A). Fig. 5(B) depicts the pressure drop between the inlet and outlet planes and computational permeability of the four types of scaffolds. The pressure drops of 400-400 scaffolds, graded 400–600 scaffolds, graded 400–800 scaffolds, and graded 400–1000 scaffolds were 0.595 Pa, 0.536 Pa, 0.421 Pa, and 0.325 Pa, respectively, while the computational permeabilities were 12.10×10^{-9} m^2, 13.43×10^{-9} m^2, 17.10×10^{-9} m^2, and 22.15×10^{-9} m^2 correspondingly. As the central pore size of scaffolds increased, a notable decrease in pressure drop was observed, which was accompanied by a corresponding increase in permeability. This indicated that the increase in central pore size within porous scaffolds could enhance the mass transport ability, even in the absence of increase in scaffold porosity. The permeability was also experimentally determined by using different fluid height (h = 30, 40, 50, 60, and 70 mm). The time of the test liquid (i.e., water) passing through the scaffolds at different fluid heights was recorded, and the fluid flow rate was calculated accordingly, as shown in Fig. 5(C). A linear trend was observed in the fluid flow rate vs. pressure drop curve for each scaffold type, which was consistent with linear Darcy's law. At a constant fluid height, as central pore size of scaffolds increased, the fluid flow exhibited an increase, resulting in a difference in mass transportation. The experimental permeability was separately calculated at different height levels, as shown in Fig. 5(D). At each fluid height, graded 400–1000 scaffold showed the highest permeability, followed by graded 400–800, graded 400–600, and finally 400-400 scaffold, indicating that scaffolds with larger pore size distributions could promote fluid conducting property, which was in good agreement with the CFD results. Besides, the experimental permeability was found to decrease with the fluid height, which may be attributed to more head loss at higher heights

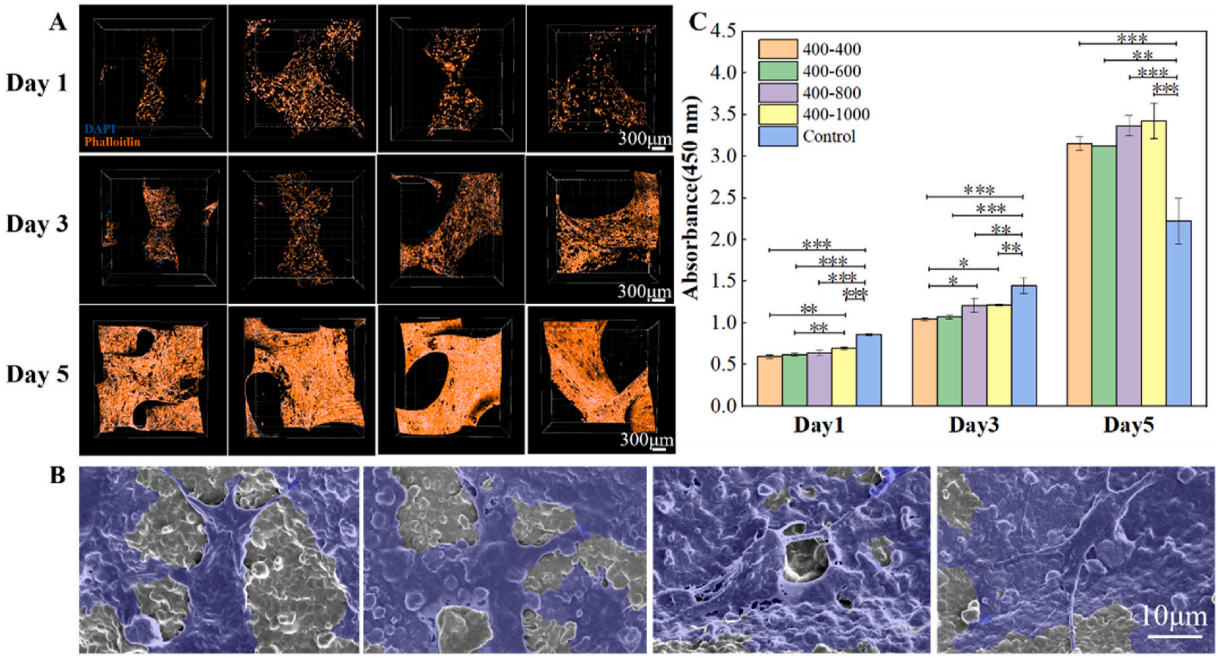

Fig. 6. *In vitro* biological assessment of uniform pore size and PSG BCP scaffolds: (A) DAPI & Phalloidin stained MC3T3-E1 cells after being cultured for 1, 3 and 5 days. (B) Morphology of MC3T3-E1 cells on BCP scaffolds after being cultured for 5 days (C) Proliferation of MC3T3-E1 cells on BCP scaffolds after incubation of 1, 3 and 5 days on BCP scaffolds (*$p < 0.05$, **$p < 0.01$, ***$p < 0.001$, $N=3$).

[67,68]. The correlation factor C is used to compare the similarity between computational and experimental permeability values (Fig. 5(E)). As the fluid height increased, the disparity between the experimental permeability and the computational widened, primarily due to the head loss effects. Notably, at the same fluid height, the experimental permeability of the uniform 400-400 scaffolds exhibited a stronger alignment with computational permeability compared to the PSG group, indicating the geometry of uniform 400-400 scaffolds possessed lower sensitivity to experimental conditions. Overall, the C values of all scaffolds in the current study ranged from 0.18 to 0.62 for fluid heights of 30 mm–70 mm. Previous studies had reported that the C values from the constant head test setup ranged from 0.06 to 0.14 and 0.12 to 0.20, respectively [67,69]. The close similarity between computational and experimental results in this study could be mainly attributed to the high reproductivity of the current DLP 3D printing process used for fabricating these structures. However, the variations between the 3D scaffold models and sintered BCP scaffolds, such as surface roughness, still resulted in significant differences between computational and experimental permeability values [50,70].

3.4. Cell adhesion and proliferation

To evaluate the cytocompatibility of BCP scaffolds, MC3T3-E1 cells were seeded on the four types of scaffolds. Fig. 6(A) shows the cytoskeleton and spreading of MC3T3-E1 cells on scaffolds after being cultured for 1, 3 and 5 days. On day 1, the cells exhibited a homogeneous distribution along the scaffold walls. As the duration of culturing was extended, a noticeable increase in cell density was observed across all scaffold groups. By day 5, the cells had established interconnections with neighboring cells and nearly formed a dense cell network that almost spanned the entire surface of the scaffolds (Fig. S4). After 5 days of culture, the cells appeared elongated and maintained their cell phenotype, with obvious filopodia extending and interacting with the scaffold surface, as shown in Fig. 6(B) and Fig. S5. These results indicated that the BCP scaffolds produced via the current process were favorable for cell attachment and adhesion. To quantitatively determine the differences in cell proliferation on these four types of scaffolds, a CCK-8 assay was performed (Fig. 6(C)). The absorbance values exhibited a consistent rise with prolonged culture time, suggesting the high proliferation of cells, which was consistent with the observations from DAPI & Phalloidin staining results. While the absorbance of graded scaffold group was slightly lower than that of the control on day 1 and day 3, the overall high absorbance values still revealed the good cytocompatibility of the BCP scaffolds. Notably, all BCP scaffolds showed significantly higher cell viability than the control on day 5, which can be attributed to the BCP scaffolds providing more space for cells and the chemical nature of BCP. The surface areas of 3D BCP scaffolds were higher than the 2D surfaces on tissue culture plastic. Besides, the presence of calcium and phosphate elements could also promote cell proliferation and bone formation [71]. Additionally, scaffolds with larger central pore sizes (graded 400–800 and graded 400–1000 scaffolds) displayed higher absorbance values across all three time points than the other two scaffold groups, indicating that scaffolds with large pores could promote cell attachment, growth and proliferation.

3.5. In vitro osteogenesis

Osteogenic differentiation, the process by which bone marrow mesenchymal stem/stomal (a.k.a skeletal stem) cells and osteoprogenitors form osteoblasts, is a critical event for bone formation during development, fracture repair, and tissue maintenance [72]. ALP activity, which serves as an early marker of osteoblastic differentiation, has been commonly used to assess early osteogenesis [73,74]. Fig. 7(A) shows ALP staining results for the four types of BCP scaffolds after cells were cultured for 7 and 14 days. After 7 days of incubation, a distinct blue precipitate was clearly observed for all scaffold groups, providing the evidence that the current BCP scaffolds could stimulate osteogenesis in the early stage of bone formation. Notably, upon extending the incubation time to 14 days, it was observed that graded 400–800 and graded 400–1000 scaffolds displayed higher expression of ALP, indicating a more active osteoblast differentiation in these two scaffold groups. To clearly show the differences, the ALP activity has been quantitively presented in Fig. 7(B). A substantial increase in ALP activity was observed across all scaffold groups from day 7 to day 14. However, no

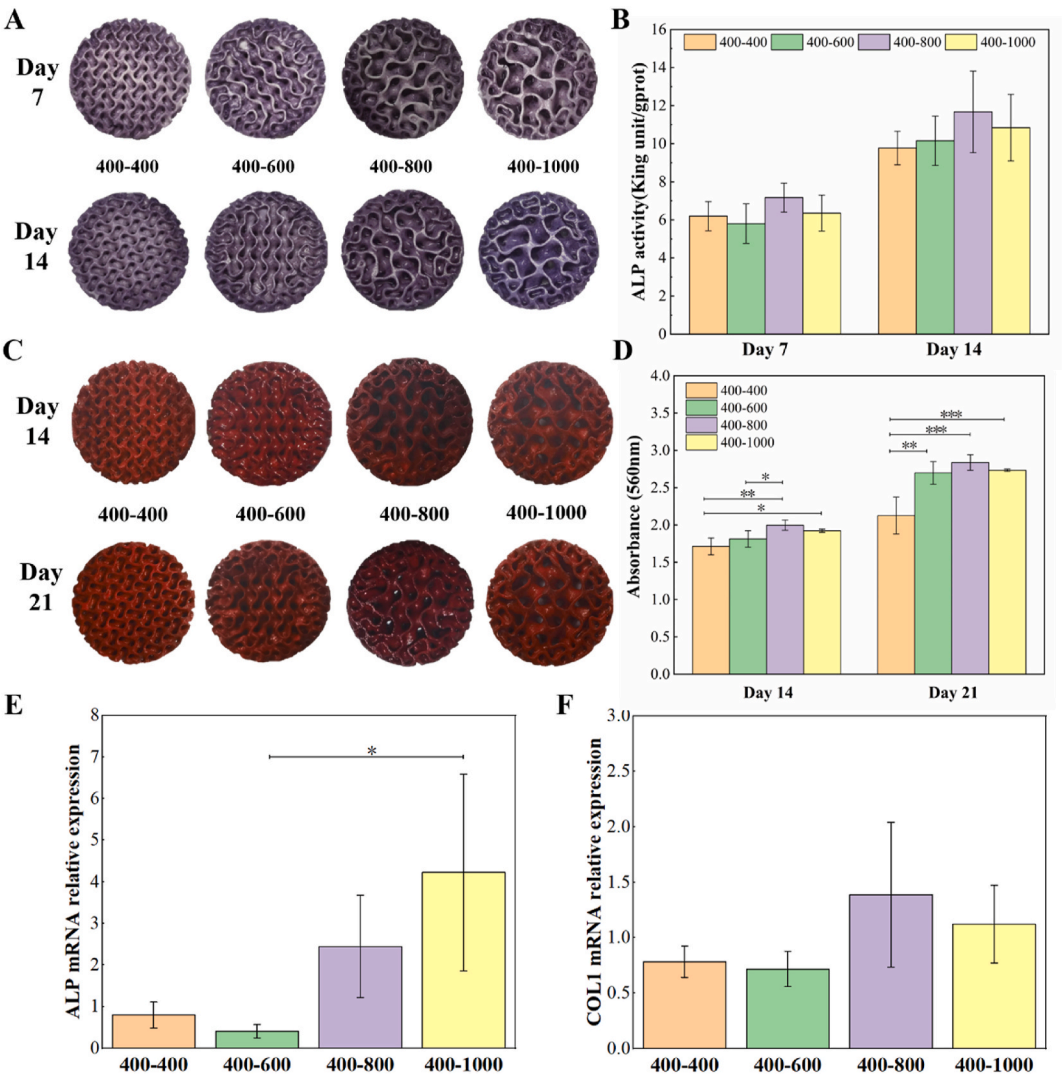

Fig. 7. *In vitro* osteogenesis of uniform pore size and PSG BCP scaffolds. ALP activities of (A) staining images and (B) quantitative analyses of MC3T3-E1 cells on four types of scaffolds after being cultured for 7 and 14 days. (B) Alizarin red activity of (C) staining images and (D) quantitative analyses of MC3T3-E1 cells on four types of scaffolds after being cultured for 14 and 21 days. Expression of osteogenic genes of (E) ALP and (F) COL 1 of MC3T3-E1 cells at day 14 of culture. (*$p < 0.05$, **$p < 0.01$, ***$p < 0.001$).

large differences were noted among the various scaffold groups at both time points. Nevertheless, two scaffold groups featuring larger central pores showed higher ALP activity than the other two scaffold groups, suggesting scaffolds with larger pores were better in promoting early osteogenesis.

To further assess the osteogenic potential of the four types of BCP scaffolds, alizarin red activity was used since it could reveal calcium deposition which is a widely recognized indicator of osteogenesis differentiation in a later stage [75,76]. Fig. 7(C) presents the results of alizarin red staining (ARS) after 14 and 21 days of incubation. At 14 days, all scaffold groups exhibited notable calcium deposition, particularly the graded 400–800 scaffolds. After 21 days of incubation, more calcium depositions were observed obviously on PSG scaffolds, with the graded 400–800 scaffolds exhibiting the most intense red color. To quantify the results, the absorbance of the dissolved solution of the alizarin red dye was measured (Fig. 7 (D)). After 14 days of incubation, graded 400–800 and 400–1000 scaffolds showed significant higher ($p < 0.01$, and $p < 0.05$, respectively) calcium deposition than 400-400 scaffolds. After 21 days of incubation, all PSG scaffolds exhibited remarkable higher calcium deposition than uniform pore size scaffolds.

The mRNA expression levels of osteogenesis-related genes (among them, ALP, and COL1) were studied after 14-day incubation of cell-scaffold samples. ALP is an early-stage osteogenic marker related to osteogenic differentiation of cells while COL1 is a late-stage osteogenic marker referring to osteogenic maturation and mineralization. As can be seen from Fig. 7(E and F), the expression of these two genes by MC3T3-E1 cells on graded 400–800 and 400–1000 scaffolds was much higher than that from cells on the other two types of BCP scaffolds, indicating good cell differentiation potential by using 400–800 and 400–1000 scaffolds in BTE. Overall, BCP scaffolds with larger pore sizes, particularly the 400–800 scaffolds, possessed an enhanced capacity for promoting the late-stage osteogenic differentiation.

3.6. *In vivo* osteogenesis and angiogenesis

To investigate the effects of different pore size gradients in BCP scaffolds on vascularization and bone regeneration efficiency *in vivo*, subcutaneous implantation of the four types of scaffolds was conducted in mice. The representative regions of interest (ROIs) of the four types of scaffolds were the transitional regions including the periphery to the center (Fig. 8(A)). After 2-week and 4-week implantation, the scaffold samples were extracted from mice and subjected to H & E staining and Goldner's Trichrome staining, and the results are shown in Fig. 8(B–C) and Fig. S6. Small blood vessels were observed in graded 400–800 and

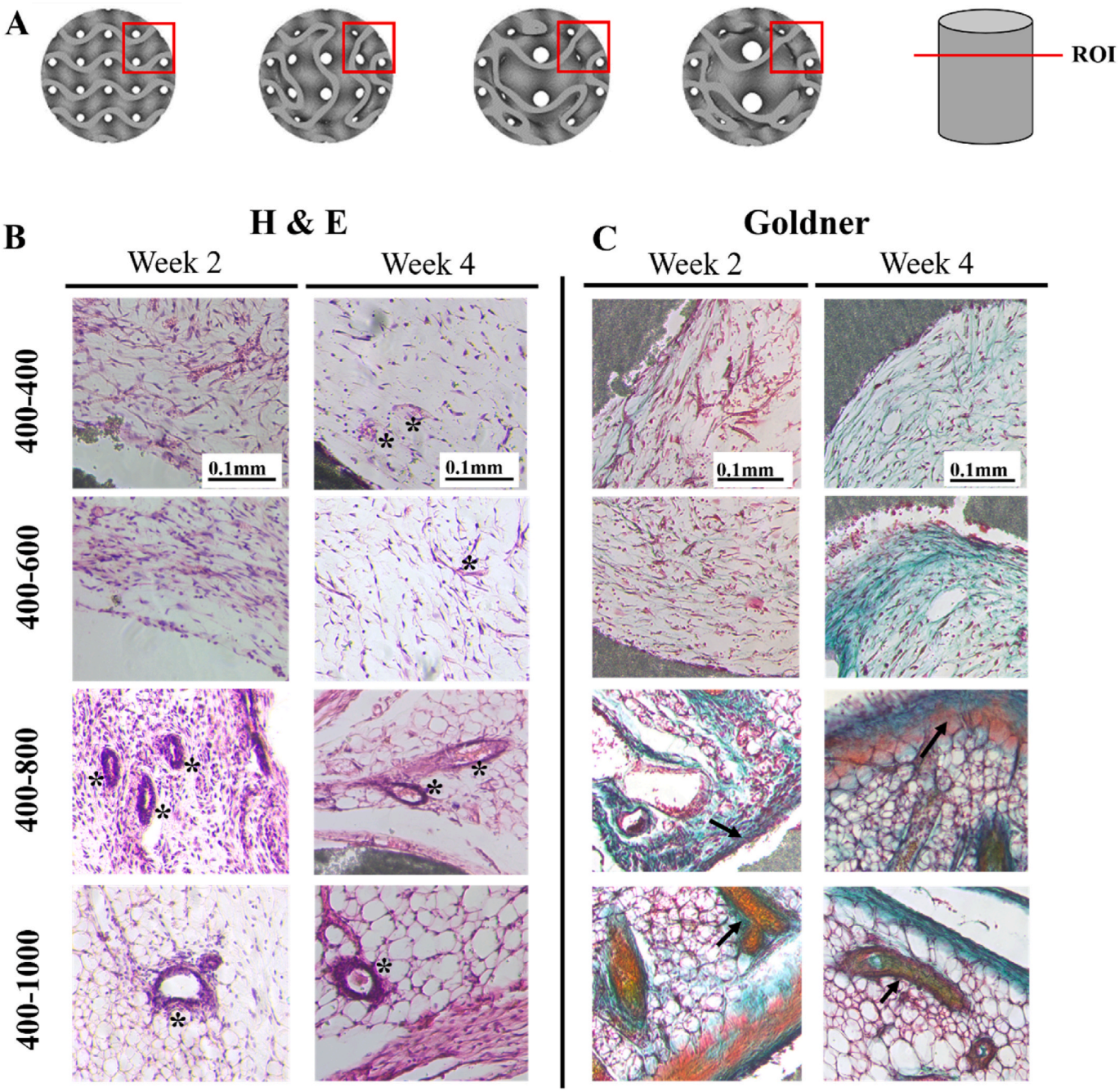

Fig. 8. Histological analysis of uniform pore size 400-400 scaffolds and graded 400–600, 400–800 and 400–1000 scaffolds after 2-week and 4-week subcutaneous implantation in mice (high magnification): (A) Illustrations for ROIs. (B) Samples after H&E staining (black star: blood vessels). (C) Samples after Goldner's Trichrome staining (black arrow: osteoid).

graded 400–1000 scaffolds two weeks after implantation, while limited vascularization was seen in the other two types of groups (Fig. 8(B)). After four weeks of implantation, the number and diameter of blood vessels in and around scaffolds increased in graded 400–800 and graded 400–1000 scaffolds. Meanwhile, small blood vessels were now visible in 400-400 scaffolds and graded 400–600 scaffolds. These results suggested that FGS BCP scaffolds with a larger central pore size had promoted angiogenesis. Wang et al. conducted a dorsal muscle embedding experiment to assess the effect of pore architecture on vascularization and concluded that scaffolds with a larger pore size exhibited larger vessel diameters [77]. Larger pores are preferred for delivering oxygen and nutrients to cells within scaffolds, thereby improving blood vessel formation. Additionally, a layer of bone lining cells (Fig. S6, pointed by red arrows) was observed on the scaffold surface of graded 400–800 and 400–1000 scaffolds, indicating the formation of bone remodeling compartment [78]. Goldner staining results also showed a better vascularization ability of graded 400–800 and 400–1000 scaffolds, which was consistent with the H&E staining results. As angiogenesis and new bone formation ability are closely interconnected processes [79], scaffolds with bigger central pore sizes may therefore enhance new bone formation. Furthermore, Osteoids were found to align around newly formed blood vessels or appeared in the scaffold edge regions(Fig. 8(C), pointed by black arrows) in graded 400–800 and graded 400–1000 scaffolds, indicating the osteogenic potential of PGS BCP scaffolds for ectopic bone regeneration.

VEGF and CD 31, commonly recognized as typical biomarkers of

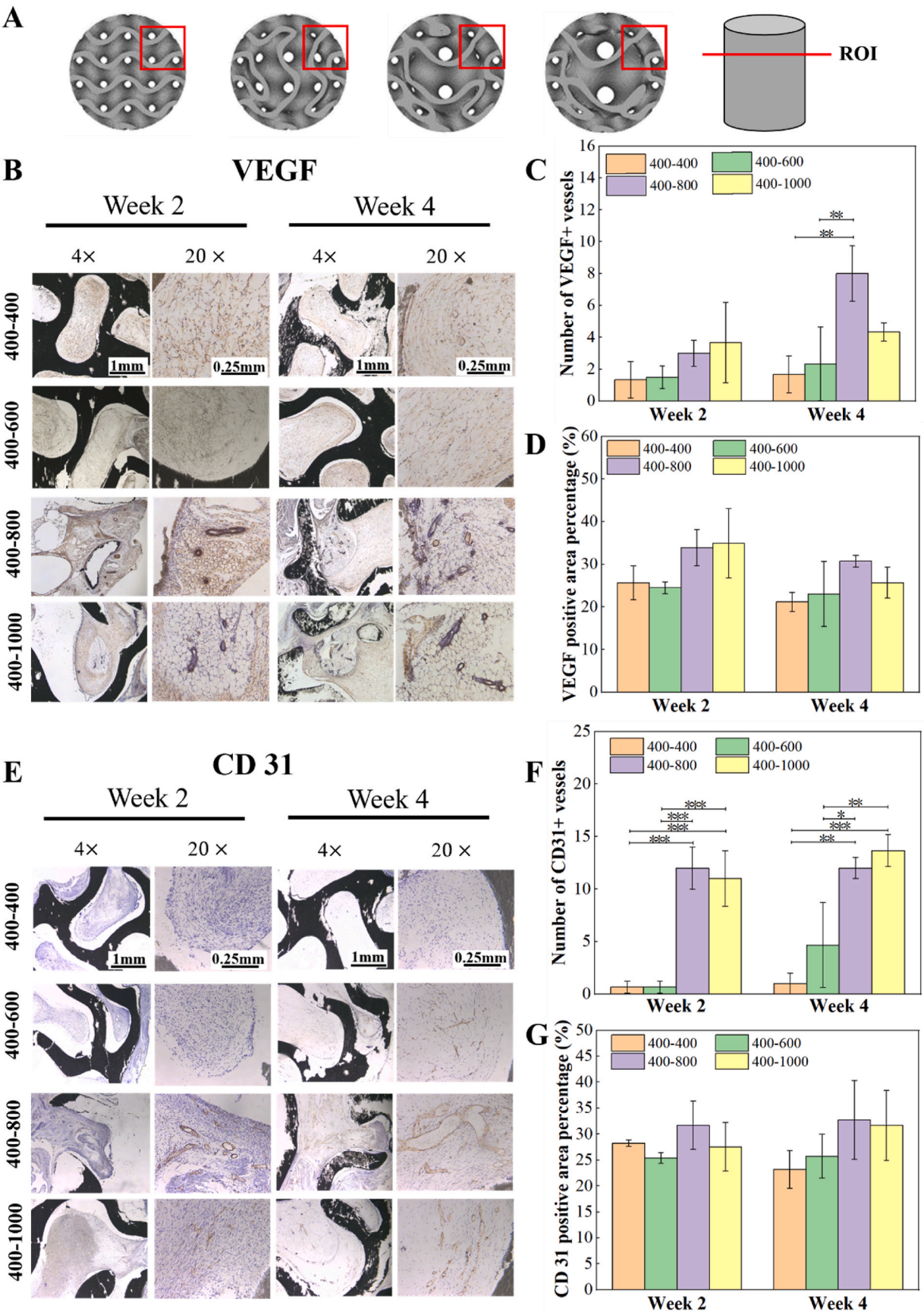

Fig. 9. Immunohistochemical analysis of uniform pore size and PSG BCP scaffolds after 2-week and 4-week subcutaneous implantation in mice: (A) Illustrations for ROIs. Results for VEGF: (B) Staining results with VEGF. (C) Number of VEGF + vessels. (D) VEGF positive area percentage. Results for CD 31: (E) Staining results with CD 31. (F) Number of CD 31 + vessels. (G) CD 31 positive area percentage (*$p < 0.05$, **$p < 0.01$, ***$p < 0.001$).

angiogenesis [80], were systematically investigated via immunohistochemical analysis (Fig. 9). The staining results (Fig. 9(B)) revealed that after two weeks of implantation, the expression of VEGF was higher in graded 400–800 and graded 400–1000 scaffolds than in the other two types of scaffolds, as evidenced by more visible VEGF + vessels and larger VEGF positive area (Fig. 9(C and D)). After four weeks of implantation, more blood vessels were present in all four types of scaffolds. Scaffolds having larger central pores displayed blood vessels with a larger diameters and greater numbers. Notably, graded 400–800 scaffolds exhibited the highest vascularization ability, as indicated by the greatest number of VEGF + vessels. Similarly, at both time points of implantation, graded 400–800 and graded 400–1000 scaffolds consistently provided the highest expression levels of CD 31, surpassing the other two types of scaffolds. This observation was supported by a greater number of CD 31 positive vessels and a larger CD 31 positive area in these two types of scaffolds (Fig. 9(E–G)). Combining these findings with the histological results could lead to the conclusion that PSG scaffolds with larger central pore sizes had facilitated vascularization and hence promoted new bone regeneration. Moreover, regions with a greater curvature change in the transitional area of scaffolds displayed the highest expression levels of both VEGF and CD 31, indicating that curvature changes within the scaffold structure may be beneficial for vascular regeneration and growth.

4. Conclusions

In the current study, uniform pore size and PSG BCP scaffolds with small pores in the periphery and large pores in the center were designed and then fabricated via DLP 3D printing. Geometrical architectures greatly affected compressive properties of BCP scaffolds. Specifically, the compressive strengths of uniform pore size 400-400, graded 400–600, and graded 400–800 scaffolds were at the same level while the compressive strength of graded 400–1000 scaffolds exhibited a large decrease, even though all types of scaffolds had the same porosity. Pore size had a direct influence on the mass transport characteristics of BCP scaffolds. With the increase of central pore size in PSG scaffolds, the maximum flow velocity in the pores increased, the pressure drop decreased while the permeability drastically increased. Furthermore, PSG BCP scaffolds with larger central pore sizes could cause better osteogenic differentiation of cells *in vitro* and neovascularization *in vivo*. Particularly, graded 400–800 scaffolds could provide enhanced osteogenesis *in vitro* and improve neovascularization and new bone formation *in vivo* while keeping their compressive properties and permeability at a high level. The current study has demonstrated that mechanical properties, mass transport properties and biological performance of BTE scaffolds could be well balanced and tuned through scaffold structural optimization and advanced manufacture via 3D printing.

CRediT authorship contribution statement

Yue Wang: Writing – original draft, Formal analysis, Data curation, Conceptualization. **Yang Liu:** Methodology, Formal analysis, Data curation. **Shangsi Chen:** Investigation, Formal analysis, Data curation. **Ming-Fung Francis Siu:** Writing – review & editing, Methodology, Investigation. **Chao Liu:** Writing – review & editing, Supervision. **Jiaming Bai:** Writing – review & editing, Supervision. **Min Wang:** Writing – review & editing, Supervision.

Ethics approval and consent to participate

All animal study procedures were followed in accordance with the Institutional Animal Care and Use Committee of Southern University of Science and Technology, China (Certificate SUSTC-JY 20190427).

Data availability

The datasets generated for this study are available on request from the corresponding authors.

Declaration of competing interest

The authors declare that they have no known competing financial interests or personal relationships that could have appeared to influence the work reported in this paper.

Acknowledgements

This work was supported by National Key R&D Program of China [2022YFE0197100], Shenzhen Science and Technology Innovation Commission [KQTD20190929172505711, KQTD20200820113012029], Guangdong Provincial Key Laboratory of Advanced Biomaterials (2022B1212010003), and Hong Kong's Research Grants Council (RGC) through research grants (17200519, 17202921, 17201622 and N_HKU749/22).

Appendix A. Supplementary data

Supplementary data to this article can be found online at https://doi.org/10.1016/j.bioactmat.2024.11.024.

References

[1] S.P. Adithya, D.S. Sidharthan, R. Abhinandan, K. Balagangadharan, N. Selvamurugan, Nanosheets-incorporated bio-composites containing natural and synthetic polymers/ceramics for bone tissue engineering, Int. J. Biol. Macromol. 164 (2020) 1960–1972.
[2] M.N. Collins, G. Ren, K. Young, S. Pina, R.L. Reis, J.M. Oliveira, Scaffold fabrication technologies and structure/function properties in bone tissue engineering, Adv. Funct. Mater. 31 (21) (2021) 2010609.
[3] M. Alonzo, F.A. Primo, S.A. Kumar, J.A. Mudloff, E. Dominguez, G. Fregoso, et al., Bone tissue engineering techniques, advances, and scaffolds for treatment of bone defects, Current opinion in biomedical engineering 17 (2021) 100248.
[4] R. Mishra, T. Bishop, I.L. Valerio, J.P. Fisher, D. Dean, The potential impact of bone tissue engineering in the clinic, Regenerative medicine 11 (6) (2016) 571–587.
[5] S. Wu, X. Liu, K.W.K. Yeung, C. Liu, X. Yang, Biomimetic porous scaffolds for bone tissue engineering, Mater. Sci. Eng. R Rep. 80 (2014) 1–36.
[6] M. Zhang, R. Lin, X. Wang, J. Xue, C. Deng, C. Feng, et al., 3D printing of Haversian bone–mimicking scaffolds for multicellular delivery in bone regeneration, Sci. Adv. 6 (12) (2020) eaaz6725.
[7] T.G. Kim, H. Shin, D.W. Lim, Biomimetic scaffolds for tissue engineering, Adv. Funct. Mater. 22 (12) (2012) 2446–2468.
[8] A. Yu, C. Zhang, W. Xu, Y. Zhang, S. Tian, B. Liu, et al., Additive manufacturing of multi-morphology graded titanium scaffolds for bone implant applications, J. Mater. Sci. Technol. 139 (2023) 47–58.
[9] R. Noroozi, F. Tatar, A. Zolfagharian, R. Brighenti, M.A. Shamekhi, A. Rastgoo, et al., Additively manufactured multi-morphology bone-like porous scaffolds: experiments and micro-computed tomography-based finite element modeling approaches, International Journal of Bioprinting 8 (3) (2022).
[10] D.R. Carter, D.M. Spengler, Mechanical properties and composition of cortical bone, Clin. Orthop. Relat. Res. 135 (1978) 192–217.
[11] M. Dziaduszewska, A. Zieliński, Structural and material determinants influencing the behavior of porous Ti and its alloys made by additive manufacturing techniques for biomedical applications, Materials 14 (4) (2021) 712.
[12] J. Manissorn, P. Wattanachai, K. Tonsomboon, P. Bumroongsakulsawat, S. Damrongsakkul, P. Thongnuek, Osteogenic enhancement of silk fibroin-based bone scaffolds by forming hybrid composites with bioactive glass through GPTMS during sol-gel process, Mater. Today Commun. 26 (2021) 101730.
[13] H. Xulin, L. Hu, Q. Liang, Y. Shuhao, W. Haoming, P. Chao, et al., 369Fabrication of 3D gel-printed β-tricalcium phosphate/titanium dioxide porous scaffolds for cancellous bone tissue engineering, International Journal of Bioprinting 9 (2) (2023).
[14] A. Sola, D. Bellucci, V. Cannillo, Functionally graded materials for orthopedic applications–an update on design and manufacturing, Biotechnol. Adv. 34 (5) (2016) 504–531.
[15] K. Leong, sC. Chua, N. Sudarmadji, W. Yeong, Engineering functionally graded tissue engineering scaffolds, Journal of the mechanical behavior of biomedical materials 1 (2) (2008) 140–152.
[16] X.-Y. Zhang, X.-C. Yan, G. Fang, M. Liu, Biomechanical influence of structural variation strategies on functionally graded scaffolds constructed with triply periodic minimal surface, Addit. Manuf. 32 (2020) 101015.

[17] S. Pagani, E. Liverani, G. Giavaresi, A. De Luca, C. Belvedere, A. Fortunato, et al., Mechanical and in vitro biological properties of uniform and graded Cobalt-chrome lattice structures in orthopedic implants, J. Biomed. Mater. Res. B Appl. Biomater. 109 (12) (2021) 2091–2103.
[18] L. Zhang, B. Wang, B. Song, Y. Yao, S.-K. Choi, C. Yang, et al., 3D printed biomimetic metamaterials with graded porosity and Tapering topology for improved cell seeding and bone regeneration, Bioact. Mater. 25 (2023) 677–688.
[19] L. Roseti, V. Parisi, M. Petretta, C. Cavallo, G. Desando, I. Bartolotti, et al., Scaffolds for bone tissue engineering: state of the art and new perspectives, Mater. Sci. Eng. C 78 (2017) 1246–1262.
[20] C. Hu, D. Ashok, D.R. Nisbet, V. Gautam, Bioinspired surface modification of orthopedic implants for bone tissue engineering, Biomaterials 219 (2019) 119366.
[21] K. Prasad, O. Bazaka, M. Chua, M. Rochford, L. Fedrick, J. Spoor, et al., Metallic biomaterials: current challenges and opportunities, Materials 10 (8) (2017) 884.
[22] J.-M. Bouler, P. Pilet, O. Gauthier, E. Verron, Biphasic calcium phosphate ceramics for bone reconstruction: a review of biological response, Acta Biomater. 53 (2017) 1–12.
[23] G. Daculsi, O. Laboux, O. Malard, P. Weiss, Current state of the art of biphasic calcium phosphate bioceramics, J. Mater. Sci. Mater. Med. 14 (3) (2003) 195–200.
[24] A. Kumar, S. Kargozar, F. Baino, S.S. Han, Additive manufacturing methods for producing hydroxyapatite and hydroxyapatite-based composite scaffolds: a review, Frontiers in Materials 6 (2019) 313.
[25] A.-N. Chen, J.-M. Wu, K. Liu, J.-Y. Chen, H. Xiao, P. Chen, et al., High-performance ceramic parts with complex shape prepared by selective laser sintering: a review, Adv. Appl. Ceram. 117 (2) (2018) 100–117.
[26] Y. Wang, S. Chen, H. Liang, Y. Liu, J. Bai, M. Wang, Digital light processing (DLP) of nano biphasic calcium phosphate bioceramic for making bone tissue engineering scaffolds, Ceram. Int. 48 (19) (2022) 27681–27692.
[27] C.-J. Bae, A. Ramachandran, K. Chung, S. Park, C.-J. Bae, A. Ramachandran, et al., Ceramic stereolithography: additive manufacturing for 3D complex ceramic structures, J. Korean Ceram. Soc. 54 (6) (2017) 470–477.
[28] J. Lai, C. Wang, M. Wang, 3D printing in biomedical engineering: processes, materials, and applications, Appl. Phys. Rev. 8 (2) (2021).
[29] Y. Wu, Q. Cao, Y. Wang, Y. Liu, X. Xu, P. Liu, et al., Optimized fabrication of DLP-based 3D printing calcium phosphate ceramics with high-precision and low-defect to induce calvarial defect regeneration, Mater. Des. 233 (2023) 112230.
[30] F. Liu, Y. Liu, X. Li, X. Wang, D. Li, S. Chung, et al., Osteogenesis of 3D printed macro-pore size biphasic calcium phosphate scaffold in rabbit calvaria, J. Biomater. Appl. 33 (9) (2019) 1168–1177.
[31] F. Bobbert, A. Zadpoor, Effects of bone substitute architecture and surface properties on cell response, angiogenesis, and structure of new bone, J. Mater. Chem. B 5 (31) (2017) 6175–6192.
[32] Q. Liu, F. Wei, M. Coathup, W. Shen, D. Wu, Effect of porosity and pore shape on the mechanical and biological properties of additively manufactured bone scaffolds, Adv. Healthcare Mater. 12 (30) (2023) 2301111.
[33] N. Top, İ. Şahin, H. Gökçe, H. Gökçe, Computer-aided design and additive manufacturing of bone scaffolds for tissue engineering: state of the art, J. Mater. Res. (2021) 1–21.
[34] S.M. Giannitelli, D. Accoto, M. Trombetta, A. Rainer, Current trends in the design of scaffolds for computer-aided tissue engineering, Acta Biomater. 10 (2) (2014) 580–594.
[35] Q. Zhang, L. Ma, X. Ji, Y. He, Y. Cui, X. Liu, et al., High-strength hydroxyapatite scaffolds with minimal surface macrostructures for load-bearing bone regeneration, Adv. Funct. Mater. 32 (33) (2022) 2204182.
[36] S. Vijayavenkataraman, L. Zhang, S. Zhang, J.Y. Hsi Fuh, W.F. Lu, Triply periodic minimal surfaces sheet scaffolds for tissue engineering applications: an optimization approach toward biomimetic scaffold design, ACS Appl. Bio Mater. 1 (2) (2018) 259–269.
[37] Z. Dong, X. Zhao, Application of TPMS structure in bone regeneration, Engineered Regeneration 2 (2021) 154–162.
[38] Y. Gür, Deformation Behaviour and Energy Absorption of 3D printed polymeric gyroid structures, Teh. Vjesn. 31 (5) (2024) 1582–1588.
[39] S. Ma, Q. Tang, Q. Feng, J. Song, X. Han, F. Guo, Mechanical behaviours and mass transport properties of bone-mimicking scaffolds consisted of gyroid structures manufactured using selective laser melting, Journal of the mechanical behavior of biomedical materials 93 (2019) 158–169.
[40] C.N. Kelly, C. Kahra, H.J. Maier, K. Gall, Processing, structure, and properties of additively manufactured titanium scaffolds with gyroid-sheet architecture, Addit. Manuf. 41 (2021) 101916.
[41] Y. Yang, T. Xu, H.-P. Bei, L. Zhang, C.-Y. Tang, M. Zhang, et al., Gaussian curvature–driven direction of cell fate toward osteogenesis with triply periodic minimal surface scaffolds, Proc. Natl. Acad. Sci. USA 119 (41) (2022) e2206684119.
[42] Y. Wang, S. Chen, H. Liang, J. Bai, M. Wang, Design and fabrication of biomimicking radially graded scaffolds via digital light processing 3D printing for bone regeneration, J. Mater. Chem. B (2023).
[43] L.E. Visscher, H.P. Dang, M.A. Knackstedt, D.W. Hutmacher, P.A. Tran, 3D printed Polycaprolactone scaffolds with dual macro-microporosity for applications in local delivery of antibiotics, Mater. Sci. Eng. C 87 (2018) 78–89.
[44] J. Fu, J. Ding, S. Qu, L. Zhang, M.Y. Wang, M.W. Fu, et al., Improved light-weighting potential of SS316L triply periodic minimal surface shell lattices by micro laser powder bed fusion, Mater. Des. 222 (2022) 111018.
[45] Y. Wang, S. Chen, H. Liang, J. Bai, M. Wang, Design and fabrication of biomimicking radially graded scaffolds via digital light processing 3D printing for bone regeneration, J. Mater. Chem. B 11 (41) (2023) 9961–9974.
[46] M. Rezapourian, I. Hussainova, Optimal mechanical properties of Hydroxyapatite gradient Voronoi porous scaffolds for bone applications — a numerical study, J. Mech. Behav. Biomed. Mater. 148 (2023) 106232.
[47] Y. Zhang, Q. Zhang, F. He, F. Zuo, X. Shi, Fabrication of cancellous-bone-mimicking β-tricalcium phosphate bioceramic scaffolds with tunable architecture and mechanical strength by stereolithography 3D printing, J. Eur. Ceram. Soc. 42 (14) (2022) 6713–6720.
[48] X. Peng, Y. Huo, G. Zhang, L. Cheng, Y. Lu, J. Li, et al., Controlled mechanical and mass-transport properties of porous scaffolds through hollow strut, Int. J. Mech. Sci. 248 (2023) 108202.
[49] J. Jiang, Y. Huo, X. Peng, C. Wu, H. Zhu, Y. Lyu, Design of novel triply periodic minimal surface (TPMS) bone scaffold with multi-functional pores: lower stress shielding and higher mass transport capacity, Front. Bioeng. Biotechnol. 12 (2024).
[50] L. Zhang, B. Song, L. Yang, Y. Shi, Tailored mechanical response and mass transport characteristic of selective laser melted porous metallic biomaterials for bone scaffolds, Acta Biomater. 112 (2020) 298–315.
[51] M. Altunbek, S.F. Afghah, A. Fallah, A.A. Acar, B. Koc, Design and 3D printing of personalized hybrid and gradient structures for critical size bone defects, ACS Appl. Bio Mater. 6 (5) (2023) 1873–1885.
[52] D. Xia, Y. Qin, H. Guo, P. Wen, H. Lin, M. Voshage, et al., Additively manufactured pure zinc porous scaffolds for critical-sized bone defects of rabbit femur, Bioact. Mater. 19 (2023) 12–23.
[53] J. Sun, X. Chen, J. Wade-Zhu, J. Binner, J. Bai, A comprehensive study of dense zirconia components fabricated by additive manufacturing, Addit. Manuf. 43 (2021) 101994.
[54] N. Travitzky, A. Bonet, B. Dermeik, T. Fey, I. Filbert-Demut, L. Schlier, et al., Additive manufacturing of ceramic-based materials, Adv. Eng. Mater. 16 (6) (2014) 729–754.
[55] O. Santoliquido, F. Camerota, A. Ortona, The influence of topology on DLP 3D printing, debinding and sintering of ceramic periodic architectures designed to replace bulky components, Open Ceramics 5 (2021) 100059.
[56] Y. Wang, S. Chen, H. Liang, Y. Liu, J. Bai, M. Wang, Digital light processing (DLP) of nano biphasic calcium phosphate bioceramic for making bone tissue engineering scaffolds, Ceram. Int. 48 (19, Part A) (2022) 27681–27692.
[57] S. Vijayavenkataraman, L.Y. Kuan, W.F. Lu, 3D-printed ceramic triply periodic minimal surface structures for design of functionally graded bone implants, Mater. Des. 191 (2020) 108602.
[58] C. Torres-Sanchez, F.R.A. Al Mushref, M. Norrito, K. Yendall, Y. Liu, P.P. Conway, The effect of pore size and porosity on mechanical properties and biological response of porous titanium scaffolds, Mater. Sci. Eng. C 77 (2017) 219–228.
[59] H. Zhao, L. Li, S. Ding, C. Liu, J. Ai, Effect of porous structure and pore size on mechanical strength of 3D-printed comby scaffolds, Mater. Lett. 223 (2018) 21–24.
[60] F. Baino, G. Magnaterra, E. Fiume, A. Schiavi, L.P. Tofan, M. Schwentenwein, et al., Digital light processing stereolithography of hydroxyapatite scaffolds with bone-like architecture, permeability, and mechanical properties, J. Am. Ceram. Soc. 105 (3) (2022) 1648–1657.
[61] R.W. Temp, M.G. Packaeser, R.V. Machry, K.S. Dapieve, M.P. Rippe, G.K.R. Pereira, et al., Characteristic fatigue strength and reliability of dental glass-ceramics: effect of distinct surface treatments–Hydrofluoric acid etching and silane treatment vs one-step self-etching ceramic primer, J. Mech. Behav. Biomed. Mater. 150 (2024) 106338.
[62] J.M. Sobral, S.G. Caridade, R.A. Sousa, J.F. Mano, RLJAb Reis, Three-dimensional plotted scaffolds with controlled pore size gradients: effect of scaffold geometry on mechanical performance and cell seeding efficiency, Acta Biomater. 7 (3) (2011) 1009–1018.
[63] K. Liu, Q. Zhou, X. Zhang, L. Ma, B. Xu, R. He, Morphologies, mechanical and in vitro behaviors of DLP-based 3D printed HA scaffolds with different structural configurations, RSC advances 13 (30) (2023) 20830–20838.
[64] L. Zhang, B. Song, L. Yang, Y.J.A.B. Shi, Tailored mechanical response and mass transport characteristic of selective laser melted porous metallic biomaterials for bone scaffolds, Acta Biomater. 112 (2020) 298–315.
[65] C. Wittkowske, G.C. Reilly, D. Lacroix, CMJFib Perrault, In vitro bone cell models: impact of fluid shear stress on bone formation, Front. Bioeng. Biotechnol. 4 (2016) 87, biotechnology.
[66] N. Rosa, R. Simoes, F.D. Magalhães, Marques ATJMe, physics. From mechanical stimulus to bone formation: a review, Med. Eng. Phys. 37 (8) (2015) 719–728.
[67] M. Zhianmanesh, M. Varmazyar, H.J.A.B.S. Montazerian, Engineering. Fluid permeability of graded porosity scaffolds architectured with minimal surfaces, ACS Biomaterials Science & EngineeringACS Biomaterials Science & Engineering 5 (3) (2019) 1228–1237.
[68] H. Montazerian, M.G.A. Mohamed, M.M. Montazeri, S. Kheiri, A.S. Milani, K. Kim, et al., Permeability and mechanical properties of gradient porous PDMS scaffolds fabricated by 3D-printed sacrificial templates designed with minimal surfaces, Acta Biomater. 96 (2019) 149–160.
[69] H. Montazerian, M. Zhianmanesh, E. Davoodi, A. Milani, M.J.M. Hoorfar, design, Longitudinal and radial permeability analysis of additively manufactured porous scaffolds: effect of pore shape and porosity, Mater. Des. 122 (2017) 146–156.
[70] D. Ali, SJAobe Sen, Computational fluid dynamics study of the effects of surface roughness on permeability and fluid flow-induced wall shear stress in scaffolds, Ann. Biomed. Eng. 46 (2018) 2023–2035.
[71] J.-P. Bonjour, Calcium and phosphate: a duet of ions playing for bone health, J. Am. Coll. Nutr. 30 (sup5) (2011), 438S-48S.
[72] C.O. Smith, R.A. Eliseev, Energy metabolism during osteogenic differentiation: the role of Akt, Stem Cell. Dev. 30 (3) (2020) 149–162.

[73] M.S. Kang, S.J. Jeong, S.H. Lee, B. Kim, S.W. Hong, J.H. Lee, et al., Reduced graphene oxide coating enhances osteogenic differentiation of human mesenchymal stem cells on Ti surfaces, Biomater. Res. 25 (2021) 1–9.
[74] J.-M. Pan, L.-G. Wu, J.-W. Cai, L.-T. Wu, M. Liang, Dexamethasone suppresses osteogenesis of osteoblast via the PI3K/Akt signaling pathway in vitro and in vivo, J. Recept. Signal Transduction 39 (1) (2019) 80–86.
[75] L. Chaudhary, A. Hofmeister, K.J.B. Hruska, Differential growth factor control of bone formation through osteoprogenitor differentiation, Bone 34 (3) (2004) 402–411.
[76] F. Norouz, R. Halabian, A. Salimi, M. Ghollasi, A new nanocomposite scaffold based on polyurethane and clay nanoplates for osteogenic differentiation of human mesenchymal stem cells in vitro, Mater. Sci. Eng. C 103 (2019) 109857.
[77] J. Wang, Y. Peng, M. Chen, X. Dai, L. Lou, C. Wang, et al., Next-generation finely controlled graded porous antibacterial bioceramics for high-efficiency vascularization in orbital reconstruction, Bioact. Mater. 16 (2022) 334–345.
[78] T. Bellido, L.I. Plotkin, A. Bruzzaniti, Chapter 3 - bone cells, in: D.B. Burr, M. R. Allen (Eds.), Basic and Applied Bone Biology, second ed., Academic Press, 2019, pp. 37–55.
[79] C.J. Percival, J.T. Richtsmeier, Angiogenesis and intramembranous osteogenesis, Dev. Dynam. 242 (8) (2013) 909–922.
[80] M. Wu, F. Chen, H. Liu, P. Wu, Z. Yang, Z. Zhang, et al., Bioinspired sandwich-like hybrid surface functionalized scaffold capable of regulating osteogenesis, angiogenesis, and osteoclastogenesis for robust bone regeneration, Materials Today Bio 17 (2022) 100458.